nature photonics

Article

https://doi.org/10.1038/s41566-023-01270-5

Mid-infrared cascade intraband electroluminescence with HgSe–CdSe core–shell colloidal quantum dots

Received: 16 December 2022

Accepted: 11 July 2023

Published online: 10 August 2023

Check for updates

Xingyu Shen, Ananth Kamath & Philippe Guyot-Sionnest ✉

Efficient infrared light sources are needed for machine vision and molecular sensing. In the visible, electroluminescence from colloidal quantum dots is highly efficient, wavelength tunable and cost effective, which motivates using the same approach in the infrared. Despite the promising performances of colloidal quantum dots light-emitting diodes in the near-infrared, mid-infrared devices show quantum efficiencies of about 0.1% due to the much weaker emission. Moreover, these devices relied exclusively on the interband transition, restricting the possible materials. Here we show electroluminescence at 5 μm using the intraband transition between $1S_e$ and $1P_e$ states within the conduction band of core–shell HgSe–CdSe colloidal quantum dots. The 4.5% quantum efficiency approaches that of commercial epitaxial cascade quantum well light-emitting diodes. The high emission efficiency and the electrical characteristics support a similar cascade process where the electrons, driven by the bias across the device, repeatedly tunnel into $1P_e$ and relax to $1S_e$ as they hop from quantum dot to quantum dot.

Mid-infrared light sources are needed for applications such as gas sensing, environmental monitoring and spectroscopy[1,2]. Thermal sources are widely used, but their broadband emission and high power consumption are poorly suited for compact and portable applications. Quantum cascade through quantum wells currently produces the most efficient mid-infrared (mid-IR, 3–5 μm) light sources[3,4]. In these cascade devices, the electrons emit a photon from the inter-sub-band transition of one quantum well, or through the interband transition of adjacent wells, and lose energy, before being driven again to the next structure and repeating the process. Quantum cascade devices based on quantum wells suffer from fast non-radiative relaxation rates. Cascade through quantum dots is predicted to result in orders-of-magnitude lower operation current and largely temperature-independent performance[5,6]. Experimental investigations have mainly used epitaxial self-assembled InAs quantum dots in the active region of the cascade structure[7–11] and, while electroluminescence and lasing are observed, they have not yet reached the predicted performance due to the difficulty in growing epitaxially uniform quantum dots over a large number of periods.

After decades of development, colloidal quantum dots (CQDs) have achieved good size and shape control, with wider tunability, narrower spectral linewidth and higher photoluminescence (PL) quantum yields than epitaxially grown quantum dots[12,13]. CQDs also benefit from solution processability and a lower refraction index, which facilitates photon extraction. CQD-based light-emitting diodes (QLEDs) in the visible region[14] are now commercialized, and they usually contain only a few layers of core–shell CQD to achieve bright luminescence but still efficient charge injection from adjacent electron and hole transport layers. Reports on infrared QLEDs include InAs[15], PbS[16–18], PbSe[19], Ag_2S[20] and HgTe[21,22]. External quantum efficiency (EQE) decreases rapidly in the infrared from ~17% at 1.4 μm (refs. 16,17,20), to 0.3% at 2.3 μm (ref. 21) and 0.1% at 4 μm (ref. 22). The pronounced decrease is similar to that observed with epitaxial LEDs and is mostly due to the decreased emission efficiency with longer wavelength.

Mid-IR interband CQDs can currently use PbSe and HgTe, and the need for a narrow-gap parent semiconductor leaves very few other options[23]. Intraband transitions provide many more options for the

James Franck Institute, The University of Chicago, Chicago, IL, USA. ✉e-mail: pgs@uchicago.edu

https://doi.org/10.1038/s41566-023-01270-5

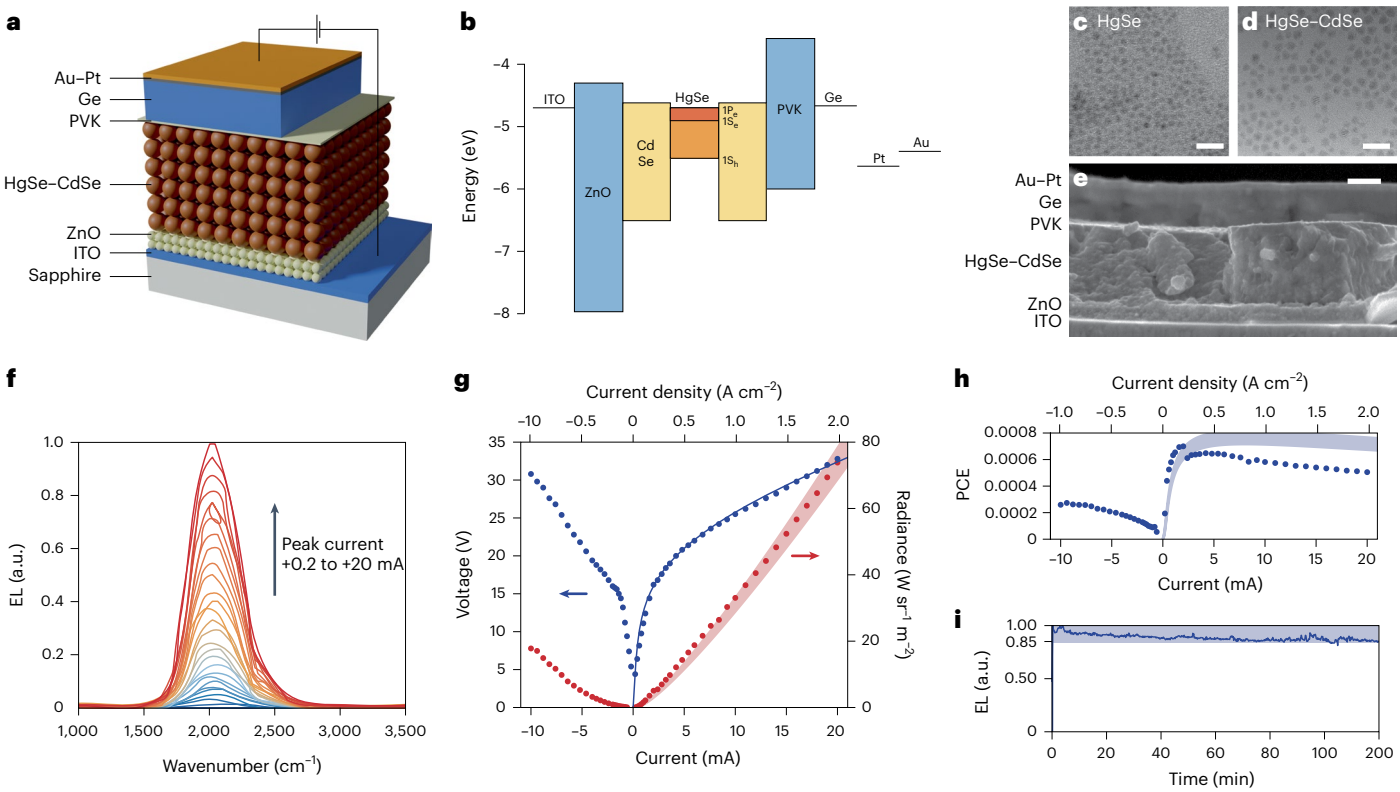

Fig. 1 | Design and electroluminescence performance of HgSe–CdSe CQDs LED. a, Schematic of the device. **b**, Energy alignment of the device. The work function values are taken from reported results[42–46]. **c**,**d**, TEM of HgSe cores (**c**) and of HgSe–CdSe CQDs (**d**). Scale bars, 20 nm. **e**, Cross-section SEM image. Scale bar, 200 nm. **f**, EL spectra at different currents. The emission peak is centred around 5 µm, which is characteristic of the intraband transition $1S_e$–$1P_e$ of the HgSe CQDs. The peak intensity grows smoothly with current. **g**, Current–voltage–radiance relationship. The device is tested using a sine wave current source at 9 kHz. The peak current, peak voltage and peak radiance are shown. The shadow area is calculated using the Poole–Frenkel model described in the text. **h**, PCE of the device. **i**, EL emission as a function of time using a peak current of +10 mA.

mid-IR. Early examples of mid-IR transitions included CdSe, InP and ZnO, and many other wide-gap CQDs should be possible[24]. Intraband excited states were initially observed to have very fast non-radiative relaxation by excitonic electron–hole Auger relaxation[25]. Slower relaxation was later obtained by extracting the holes and using shells to diminish non-radiative energy transfer to ligand vibrations[26]. Mid-IR intraband luminescence was then observed with double photoexcitation of CdS and CdSe CQDs[27] and direct photoexcitation of n-doped CQDs of HgS[28], HgSe[29] and Ag_2Se[30]. The n-doped HgSe CQDs have an intraband emission efficiency of about 0.07% with the cores, which is similar to mid-IR interband HgTe. This increases to 0.1% in thin-shell HgSe–CdSe[31], and to 2% with thick-shell HgSe–CdS[32]. CQD intraband transitions now provide the brightest soluble mid-IR chromophores and could therefore be attractive for mid-IR electroluminescent QLEDs.

In efficient QLEDs studied so far, the electroluminescence (EL) arises from electron–hole recombination and it cannot be more efficient than PL. As such, an HgTe QLED p–n junction reached an EQE of ~0.1% at low current[22]. Considering the small mid-IR energy (0.25–0.4 eV), the cascade mechanism could be realized with a moderate electric field through an emissive layer and gave much better quantum efficiency. This consideration led us to explore the concept of cascade CQDs electroluminescence using core–shell HgSe–CdSe CQDs.

Results

Device structure

A schematic of a device structure is shown in Fig. 1a. It consists of a sapphire substrate with a 40 nm indium tin oxide (ITO) layer as one electrode coated with a 60 nm ZnO layer by spin coating, which is subsequently annealed. A tentative energy alignment diagram of the structure is shown in Fig. 1b. The ~500 nm CQD layer is made by multiple drop casting and ligand exchange. The HgSe–CdSe CQD synthesis and characterization[33] follows that of previous work on HgSe–CdS core shells[32]. Figure 1c,d shows the transmission electron microscopy (TEM) images of the HgSe CQD cores and the core–shells. The intraband PL is tunable by the size of cores[29]. HgSe CQDs with core sizes of about 4.8 nm are chosen since they have the brightest intraband emission around 5 µm. The CdSe shell is about three monolayers thick. On top of the CQD layer, a 10 nm poly(9-vinylcarbazole) (PVK) layer is spin coated. Then, a 200 nm Ge layer is evaporated. Finally, the top electrode is evaporated through a shadow mask, with 15 nm Pt followed by 20 nm Au. Each device area is measured by optical microscopy, and they are around 1 mm^2. The light is extracted from the ITO side. A cross-section scanning electron microscopy (SEM) image of the device is shown in Fig. 1e.

ZnO and PVK layers are used to inject electrons and holes into the CQD layer. We found that removing either the ZnO or PVK reduced the emission efficiency by several fold. The Ge layer is conductive at room temperature. It was added to provide a quarter-wave distance between the metal electrode and the middle of the CQD layer and this improved the emission efficiency 2–3-fold. The Pt–Au electrode improved the lifetime of the devices compared to just Au. More details of device structure are presented in the Supplementary Information.

EL measurements

The EL is excited by a current source producing a sine wave from 0 mA to a certain peak current at 9 kHz, with the frequency being limited by the current source. The emitted light is sent through a step-scan Michelson interferometer and collected by an MCT detector. The signal is then analysed by a lock-in amplifier. The high modulation frequency

https://doi.org/10.1038/s41566-023-01270-5

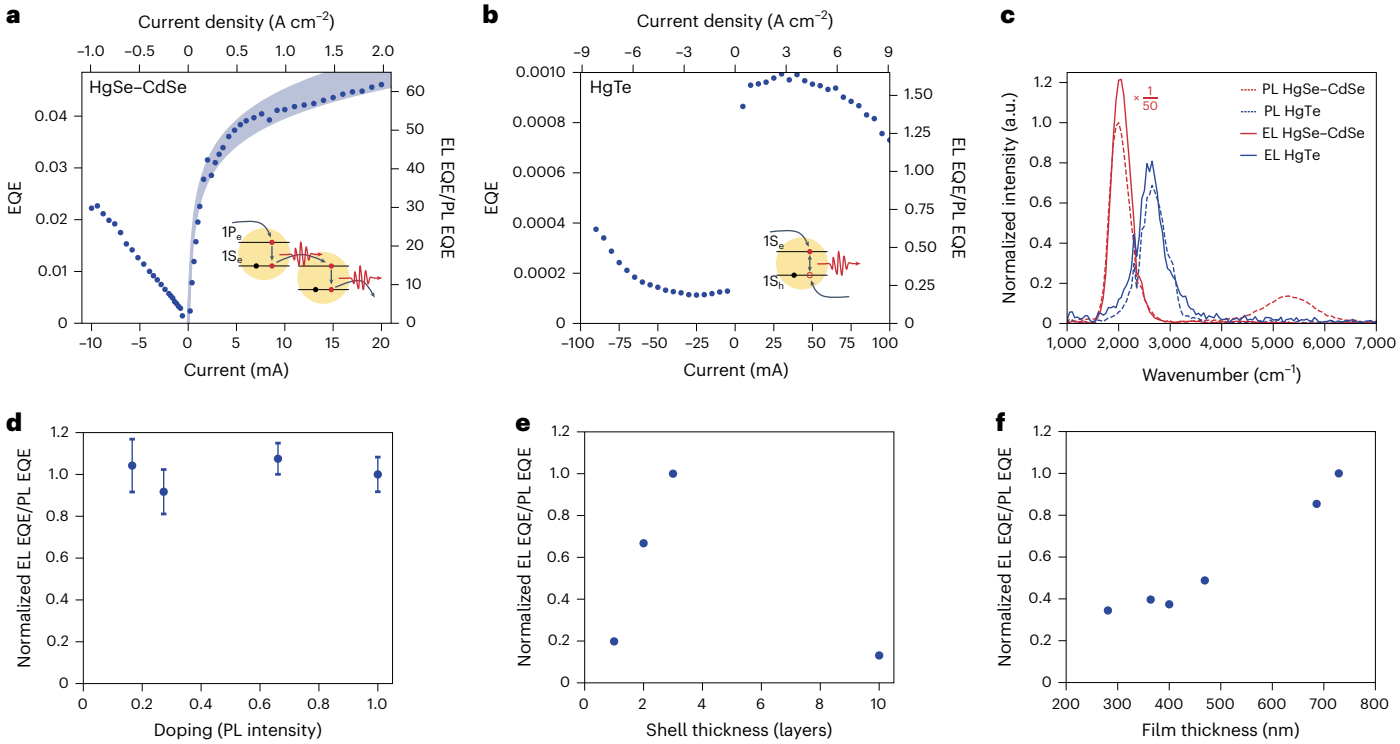

Fig. 2 | Quantum efficiency of HgSe–CdSe and HgTe devices and mechanism discussion. a, EQE of the HgSe–CdSe device versus current. **b**, EQE of the HgTe device versus current. **c**, PL and EL spectra of HgSe–CdSe and HgTe devices. Spectra are normalized to the number of absorbed photons or injected electrons and the intensities are comparable, noting that the EL signal is divided by 50 for the HgSe–CdSe device. **d**, Normalized EL EQE/PL EQE ratio of CQDs with different doping. The error bars come from fitting each emission spectrum with a Gaussian peak. **e**, Normalized EL EQE/PL EQE ratio of CQDs with different shell thickness. **f**, Normalized EL EQE/PL EQE ratio of CQDs with different CQD layer thickness.

allows measurement of the EL and reduces thermal emission to the extent that it is not observable in the spectra. Figure 1f shows the EL spectra at different currents. The emission is characteristic of the intraband transition $1S_e$–$1P_e$ of the HgSe CQDs. It peaks around 2,000 cm^{-1} (5 µm) with a full-width at half-maximum (FWHM) of about 440 cm^{-1}. The peak centre and the FWHM are shown in Supplementary Fig. 7c,d. The peak position blueshifts by about 50 cm^{-1} at small current, and does not change much at larger current, while the FWHM increases little with current, from 420 cm^{-1} to 450 cm^{-1}. The peak current, peak voltage and peak radiance are shown in Fig. 1g. Since both current and bias contribute to increasing the EL, the radiance appears most linear on a plot in terms of the electrical power, as shown in the Supplementary Information. The device works with a large voltage, with +20 V at +5 mA and +32 V at +20 mA. The device is not Ohmic, with the voltage increasing fast for small current and more slowly for larger current. The device also shows a weak rectification with a smaller voltage for the same current in forward bias, defined as the positive bias on the PVK. The EL signal is also stronger in forward bias, and it increases with current, with a peak radiance of 75 W sr^{-1} m^{-2} at +20 mA. The power conversion efficiency (PCE) of the device is shown in Fig. 1h. The PCE is 0.07% at +2 mA and average electrical power 16 mW, and drops only to 0.05% at +20 mA and average electrical power 320 mW. The device stability, tested using a +10 mA sine wave current at 9 kHz, is shown in Fig. 1i. The EL signal drops 15% over 2 h and the voltage increases from 30 V to 40 V.

The EL EQE is shown in Fig. 2a. The EL EQE increases fast at small current and slowly at large current, reaching about 4.5% at +20 mA. The device PL EQE is recorded using an 808 nm laser modulated by a sine wave at 90 kHz. In contrast to the EL, the PL shows some interband emission in addition to the intraband emission. The PL intraband EQE is defined as the number of intraband photons emitted per 808 nm photons absorbed and was determined to be 0.075%. The EL EQE is therefore up to 60 times larger than the PL EQE.

Discussion

The EL performance is vastly improved compared to the previous interband HgTe p–n QLED[22], which achieved an EQE of 3.4×10^{-4} and a PCE of 5.0×10^{-5} for an average electrical power of 80 mW. It is also much better than for a similar structure using interband HgTe CQDs, as shown in Fig. 2b. However, the HgSe–CdSe intraband device shows an approximately similar PL efficiency to the HgTe interband device. The much brighter EL than PL suggests a cascade mechanism for the EL emission, where one injected carrier gives rise to multiple emissions as it falls down the device from quantum dot to quantum dot. Given the 0.25 eV energy gap between $1P_e$ and $1S_e$ states, the working voltage of up to 20 V across ~50–100 dot layers gives plenty of potential energy for electrons to tunnel many times from the $1S_e$ state of one quantum dot into the $1P_e$ state of another quantum dot downstream, and relax each time with some radiative probability. This cascade mechanism, which is well established for epitaxial quantum wells, is a new mechanism for QLEDs. The striking difference with the HgTe interband results, which has a similar energy gap, also suggests that this cascade emission may be favoured with the sparse level structure of the intraband states.

New bright solution-processable non-thermal infrared sources with fast response may open up exciting possibilities, such as pixelated devices for infrared scene projection and mass production of optical gas sensors. There is also much effort in making QLEDs to achieve lasing in the visible region[34]. Electrically driven amplified spontaneous emission was realized recently[35]. Several favourable properties of the intraband transitions, such as low state degeneracy, the possibility of reduced laser threshold at the 1 electron per dot

doping level[36,37] and reduced Auger rate of the intraband transition, will justify exploring this system further towards electrically pumped infrared lasing.

In forward bias, the current–voltage (I–V) curve of ITO–ZnO–QDs–PVK–Au can be approximated by $I \propto V^n$, with $n \approx 2.8$ after a small turn-on voltage. Such a power law exists in space charge-limited transport with traps and it has been invoked in visible-light-emitting CdSe–ZnS QLEDs[38,39]. In these visible-light-emitting devices, the reported values of n are 5–9. The Mott–Gurney model gives an exponent $n = 2$, while for an exponential tail of trap energies of the form $\exp(\frac{-E}{kT_c})$, the Mark–Helfrich model gives $n = \frac{T_c}{T} + 1$ (ref. 39), where E is energy, T is temperature and Tc is the characteristic temperature for trap distribution. However, the space charge model only applies if the material is sufficiently insulating and this is not necessarily the case with infrared-gap CQD films. Indeed, the values obtained for doping and mobility of the HgSe–CdSe layer (Supplementary Information) show that the space charge-limited current would be three orders of magnitude too small from 10 V to 1 V bias.

An alternative transport model is a field-driven hopping transport, such as the Poole–Frenkel model[40,41], which prescribes a conductivity given by $\sigma_0(T) \propto \exp\left(\frac{q}{kT}\sqrt{\frac{qE}{\pi\varepsilon_{QD}}}\right)$, where E is a uniform electric field across the material, ε_{QD} is the permittivity of the CQD layer and is taken to be $4\varepsilon_0$. Combining a 350 Ω series resistance and a 2,500 Ω shunt resistance, the Poole–Frenkel model gives a very good fit of the I–V curve in forward bias, as shown in Fig. 1g.

In analogy to the case of single electron–hole recombination, the EL EQE for the cascade device is expressed as $\eta_{EL} = \eta_{rec} \times \left(\frac{eV}{E_g}\right) \times \eta_{rad} \times \eta_{ext}$ $\frac{eV}{E_g}$ is the maximum possible cascade gain, such that for every voltage increment equal to the energy gap (0.25 eV) there would be an electron transferring from $1S_e$ to $1P_e$. η_{rec} is a downward correction to that maximum possible gain, which is effectively the probability of the electron being injected in the $1P_e$ state. η_{rad} is the probability of $1P_e$–$1S_e$ emission, η_{ext} is the photon extraction probability. Assuming the same η_{ext} for EL and PL, the photoluminescence EQE is $\eta_{PL} = \eta_{rad} \times \eta_{ext}$. The EL radiance is calculated as Radiance $= \frac{I \times \eta_{EL}}{\pi \times A} = \frac{\eta_{PL}}{\pi \times A} \times \eta_{rec} \times I \times \left(\frac{eV}{E_g}\right)$, where π is the solid angle for a Lambertian emitter, A is the device area and I and V are the current and voltage through the junction. The radiance versus current is bracketed using η_{rec} between 0.68 and 0.60. This corresponds to a photon emitted for every 0.36–0.41 V additional bias. The EQE and PCE calculated using the same parameters are shown in Figs. 2a and 1h. The interpretation is that there is good transfer of the electrons from $1S_e$ of one dot to the $1P_e$ state of the dot as the electrons cascade down from the cathode to the anode. This is a surprising result given the simplicity and imperfection of the CQD layer compared to the elaborately engineered multiple quantum well structures used in quantum cascade.

We performed further experiments to explore the effects of doping, shell thickness and CQD film thickness. Regarding the doping of QDs, this is controlled by the amount of cadmium acetate added in a final reheating of the CQD solution[32]. We found that, as the intraband PL increases by a factor of ten across samples with stronger doping, the EL follows the same trend, such that the ratio of EL EQE to PL EQE is similar for all the samples shown in Fig. 2d. This indicates that the intraband EL is also proportional to the number of doped dots. This can be expected since, when an electron tunnels from $1S_e$ of one dot to a dot downstream, the branching ratio to $1P_e$ is higher if there is already an electron blocking $1S_e$, because of the combination of electron–electron repulsion, statistical benefits and drive potential. However, we do not know the doping within the devices precisely enough to state whether the optimum doping is at 1 or 2 electrons per dot. This is because spectroscopic measurements with the finished device are too imprecise to determine the doping of the layer.

With shell thickness, the EL optimum is at three monolayers of CdSe. This must reflect a compromise between emission efficiency, tunnelling and doping. While intraband PL increases with shell thickness, the thick shell (ten monolayers of CdSe) is much harder to n dope than the thinner shell samples (1, 2, 3 monolayers). The intraband EL EQE to PL EQE ratio of devices made with different shell thicknesses is shown in Fig. 2e. It first increases with shell thickness and then drops for the thickest shell.

With device thickness, it appears that increasing the thickness of the CQD layer increases the EL EQE to PL EQE ratio. This is consistent with the need for a higher voltage to produce the same current, and this supports the cascade mechanism. More details of the effects of doping, shell thickness and CQD film thickness are presented in the Supplementary Information.

In summary, we demonstrated the intraband electroluminescence at 5 µm from n-doped core–shell HgSe–CdSe CQDs in a simple structure and showed that cascade emission is an attractive possibility for small energy gap CQDs. The device showed an EQE of 4.5% at 2 A cm^{-2}, while the power efficiency was 0.05%. These values are within range of those obtained with epitaxial quantum well cascade LEDs, while the radiance is smaller, limited by the power dissipation and device damage. Compared with epitaxial quantum well cascade LEDs or lasers, which usually have currents of kA cm^{-2}, the cascade mid-IR QLED works at low currents of A cm^{-2}. Refinements of the synthesis and film processing will probably improve the photoluminescence of the CQDs, and this will directly lead to even brighter devices. Different core sizes will allow targeting of different wavelengths. Moreover, many other CQD systems should exhibit similar intraband transitions, including the InP–ZnS currently applied to commercial visible displays, and the cascade mid-IR QLED design could then be extended to lower toxicity systems.

Online content

Any methods, additional references, Nature Portfolio reporting summaries, source data, extended data, supplementary information, acknowledgements, peer review information; details of author contributions and competing interests; and statements of data and code availability are available at https://doi.org/10.1038/s41566-023-01270-5.

References

1. Jung, D., Bank, S., Lee, M. L. & Wasserman, D. Next-generation mid-infrared sources. *J. Opt.* **19**, 123001 (2017).
2. Krier, A; et al. in *Mid-Infrared Optoelectronics* (eds Tournie, E. & Cerutti, L.) 59–90 (Elsevier, 2020).
3. Vitiello, M. S., Scalari, G., Williams, B. & De Natale, P. Quantum cascade lasers: 20 years of challenges. *Opt. Express* **23**, 5167–5182 (2015).
4. Vurgaftman, I. et al. Interband cascade lasers. *J. Phys. D* **48**, 123001 (2015).
5. Wingreen, N. S. & Stafford, C. A. Quantum-dot cascade laser: proposal for an ultralow-threshold semiconductor laser. *IEEE J. Quantum Electron.* **33**, 1170–1173 (1997).
6. Dmitriev, I. & Suris, R. Quantum dot cascade laser: arguments in favor. *Physica E* **40**, 2007–2009 (2008).
7. Zhuo, N. et al. Quantum dot cascade laser. *Nanoscale Res. Lett.* **9**, 144 (2014).
8. Zhuo, N. et al. Room temperature continuous wave quantum dot cascade laser emitting at 7.2 µm. *Opt. Express* **25**, 13807–13815 (2017).
9. Ulbrich, N. et al. Midinfrared intraband electroluminescence from AlInAs quantum dots. *Appl. Phys. Lett.* **83**, 1530–1532 (2003).
10. Liverini, V., Bismuto, A., Nevou, L., Beck, M. & Faist, J. Midinfrared electroluminescence from InAs/InP quantum dashes. *Appl. Phys. Lett.* **97**, 221109 (2010).

11. Wasserman, D., Ribaudo, T., Lyon, S., Lyo, S. & Shaner, E. Room temperature midinfrared electroluminescence from InAs quantum dots. *Appl. Phys. Lett.* **94**, 061101 (2009).
12. Efros, A. L. & Brus, L. E. Nanocrystal quantum dots: from discovery to modern development. *ACS Nano* **15**, 6192–6210 (2021).
13. Bayer, M. Bridging two worlds: colloidal versus epitaxial quantum dots. *Ann. Phys.* **531**, 1900039 (2019).
14. Shirasaki, Y., Supran, G. J., Bawendi, M. G. & Bulović, V. Emergence of colloidal quantum-dot light-emitting technologies. *Nat. Photonics* **7**, 13–23 (2013).
15. Tessler, N., Medvedev, V., Kazes, M., Kan, S. & Banin, U. Efficient near-infrared polymer nanocrystal light-emitting diodes. *Science* **295**, 1506–1508 (2002).
16. Supran, G. J. et al. High-performance shortwave-infrared light-emitting devices using core–shell (PbS–CdS) colloidal quantum dots. *Adv. Mater.* **27**, 1437–1442 (2015).
17. Gong, X. et al. Highly efficient quantum dot near-infrared light-emitting diodes. *Nat. Photonics* **10**, 253–257 (2016).
18. Pradhan, S. et al. High-efficiency colloidal quantum dot infrared light-emitting diodes via engineering at the supra-nanocrystalline level. *Nat. Nanotechnol.* **14**, 72–79 (2019).
19. Steckel, J. S., Coe-Sullivan, S., Bulović, V. & Bawendi, M. G. 1.3 μm to 1.55 μm tunable electroluminescence from PbSe quantum dots embedded within an organic device. *Adv. Mater.* **15**, 1862–1866 (2003).
20. Vasilopoulou, M. et al. Efficient colloidal quantum dot light-emitting diodes operating in the second near-infrared biological window. *Nat. Photonics* **14**, 50–56 (2020).
21. Qu, J. et al. Electroluminescence from nanocrystals above 2 μm. *Nat. Photonics* **16**, 38–44 (2022).
22. Shen, X., Peterson, J. C. & Guyot-Sionnest, P. Mid-infrared HgTe colloidal quantum dot LEDs. *ACS Nano* **16**, 7301–7308 (2022).
23. Lu, H., Carroll, G. M., Neale, N. R. & Beard, M. C. Infrared quantum dots: progress, challenges, and opportunities. *ACS Nano* **13**, 939–953 (2019).
24. Guyot-Sionnest, P., Shim, M. & Wang, C. in *Nanocrystal Quantum Dots* (ed. Klimov, V. I.) 133–146 (CRC Press, 2017).
25. Klimov, V. I. & McBranch, D. W. Femtosecond 1P-to-1S electron relaxation in strongly confined semiconductor nanocrystals. *Phys. Rev. Lett.* **80**, 4028 (1998).
26. Pandey, A. & Guyot-Sionnest, P. Slow electron cooling in colloidal quantum dots. *Science* **322**, 929–932 (2008).
27. Jeong, K. S. & Guyot-Sionnest, P. Mid-infrared photoluminescence of CdS and CdSe colloidal quantum dots. *ACS Nano* **10**, 2225–2231 (2016).
28. Shen, G. & Guyot-Sionnest, P. HgS and HgS/CdS colloidal quantum dots with infrared intraband transitions and emergence of a surface plasmon. *J. Phys. Chem. C* **120**, 11744–11753 (2016).
29. Deng, Z., Jeong, K. S. & Guyot-Sionnest, P. Colloidal quantum dots intraband photodetectors. *ACS Nano* **8**, 11707–11714 (2014).
30. Bera, R., Choi, D., Jung, Y. S., Song, H. & Jeong, K. S. Intraband transitions of nanocrystals transforming from lead selenide to self-doped silver selenide quantum dots by cation exchange. *J. Phys. Chem. Lett.* **13**, 6138–6146 (2022).
31. Shen, G. & Guyot-Sionnest, P. HgTe/CdTe and HgSe/CdX (X= S, Se, and Te) core/shell mid-infrared quantum dots. *Chem. Mater.* **31**, 286–293 (2018).
32. Kamath, A., Melnychuk, C. & Guyot-Sionnest, P. Toward bright mid-infrared emitters: thick-shell n-type HgSe/CdS nanocrystals. *J. Am. Chem. Soc.* **143**, 19567–19575 (2021).
33. Kamath, A., Schaller, R. D. & Guyot-Sionnest, P. Bright fluorophores in the second near-infrared window: HgSe/CdSe quantum dots. *J. Am. Chem. Soc.* **145**, 10809–10816 (2023).
34. Jung, H. et al. Two-band optical gain and ultrabright electroluminescence from colloidal quantum dots at 1000 A cm^{-2}. *Nat. Commun.* **13**, 3734 (2022).
35. Ahn, N. et al. Electrically driven amplified spontaneous emission from colloidal quantum dots. *Nature* **617**, 79–85 (2023).
36. Wang, C., Wehrenberg, B. L., Woo, C. Y. & Guyot-Sionnest, P. Light emission and amplification in charged CdSe quantum dots. *J. Phys. Chem. B* **108**, 9027–9031 (2004).
37. Wu, K., Park, Y.-S., Lim, J. & Klimov, V. I. Towards zero-threshold optical gain using charged semiconductor quantum dots. *Nat. Nanotechnol.* **12**, 1140–1147 (2017).
38. Cho, K.-S. et al. High-performance crosslinked colloidal quantum-dot light-emitting diodes. *Nat. Photonics* **3**, 341–345 (2009).
39. Hikmet, R., Talapin, D. & Weller, H. Study of conduction mechanism and electroluminescence in CdSe/ZnS quantum dot composites. *J. Appl. Phys.* **93**, 3509–3514 (2003).
40. Sze, S. M. & Ng, K. K. *Physics of Semiconductor Devices* 3rd edn, 227–229 (John Wiley & Sons, 2007).
41. Lei, S. et al. Temperature-dependent transition of charge transport in core/shell structured colloidal quantum dot thin films: from Poole–Frenkel emission to variable-range hopping. *Appl. Phys. Lett.* **121**, 063301 (2022).
42. Nehate, S. D., Prakash, A., Mani, P. D. & Sundaram, K. B. Work function extraction of indium tin oxide films from MOSFET devices. *ECS J. Solid State Sci. Technol.* **7**, P87 (2018).
43. Yang, X. et al. Iodide capped PbS/CdS core-shell quantum dots for efficient long-wavelength near-infrared light-emitting diodes. *Sci. Rep.* **7**, 14741 (2017).
44. Wu, Y. et al. Widely applicable phosphomolybdic acid doped poly(9-vinylcarbazole) hole transport layer for perovskite light-emitting devices. *RSC Adv.* **9**, 30398–30405 (2019).
45. Sholin, V. et al. All-inorganic CdSe/PbSe nanoparticle solar cells. *Sol. Energy Mater. Sol. Cells* **92**, 1706–1711 (2008).
46. Chen, M. & Guyot-Sionnest, P. Reversible electrochemistry of mercury chalcogenide colloidal quantum dot films. *ACS Nano* **11**, 4165–4173 (2017).

Methods

Chemicals

Chemicals used were as follows: mercury(II) chloride ($HgCl_2$, Sigma-Aldrich, ≥99.5%, catalogue no. 215465, 100 g), oleylamine (Sigma-Aldrich, catalogue no. 909831, 500 g), bis(trimethylsilyl)selenide ($(TMS)_2Se$, Gelest, catalogue no. SIB1871.0, 1 g), cadmium acetate hydrate (Aldrich, 99.99+%, catalogue no. 229490, 25 g), (di-*n*-dodecyl) dimethylammonium bromide (DDAB, Alfa Aesar, 98+%, catalogue no. B22839), zinc acetate dehydrate (Sigma-Aldrich, ≥99.0%, catalogue no. 96459, 250 g), potassium hydroxide pellets (Sigma-Aldrich, 85+%, catalogue no. 221473, 500 g), 1,2-ethanedithiol (Sigma-Aldrich, ≥98.0%, catalogue no. 02390, 100 ml), poly(9-vinylcarbazole) (PVK, Aldrich, catalogue no. 18260-5), poly(diallyldimethylammonium chloride) (very low molecular weight, 35 wt% in water, Aldrich, catalogue no. 522376, 25 ml), chlorobenzene (Sigma-Aldrich, ≥99.5%, catalogue no. 23570, 2.5 l), tetrachloroethylene (TCE, Sigma-Aldrich, ≥99.0%, catalogue no. 443786, 2.5 l), chloroform (Fisher, catalogue no. C606-4), ethanol (Decon, catalogue no. UN1170), 2-propanol (IPA, Fisher, catalogue no. A451-4), acetone (Fisher, catalogue no. A18-4), methanol (Fisher, catalogue no. A452-4)

Thin-shell HgSe–CdSe QD synthesis

Thin-shell HgSe–CdSe QDs were synthesized using a reported process[33]. The following protocol yielded ~20 mg of HgSe cores. Briefly, $HgCl_2$ (0.1 mmol, 27 mg) was added to a three-neck flask with 5 ml of oleylamine. The flask was equipped with a stir bar, rubber sleeve stoppers with a thermocouple attached and connected to an argon Schlenk-line manifold. The flask was heated at 100 °C for ~30–60 min. The temperature was then set to 90 °C. Then, 0.5 ml of 0.2 M $(TMS)_2Se$ solution was injected swiftly into the flask. At 15 s, a calculated volume of 0.2 M cadmium acetate ($Cd(OAc)_2$) solution ('0Cd') was injected over a period of ~15 s. After 5 min, a calculated volume of 0.2 M $(TMS)_2Se$ solution ('1Se') was injected over a period of ~15 s. Subsequent half-cycles were performed until '3Cd', with a 2 min reaction time for Se cycles and 5 min reaction time for Cd cycles. This led to QDs with a diameter ~7 nm.

The stock solution was transferred into a glass vial and stored in a freezer. The solution could be stored for several months with no observable change.

HgSe–CdSe solution cleaning

A 80 µl HgSe–CdSe solution was diluted by 0.5 ml of TCE. Ethanol was added dropwise until the solution became turbid. The solution was centrifuged. The supernatant was discarded, and the precipitate was dissolved in 1 ml of TCE. Cadmium acetate hydrate was added to the solution to n dope the sample. Excess cadmium acetate hydrate did not dissolve. The solution was heated to boiling for 1 min. After cooling down, 80 µl of 0.1 M DDAB solution in isopropanol was added to aid redispersion. Ethanol was then added to precipitate the quantum dots. The solution was centrifuged. The supernatant was discarded and the precipitate was dissolved in 0.5 ml of TCE for fabrication.

ZnO nanoparticles synthesis

ZnO nanoparticles were synthesized in a similar process to that previously reported[21]. A 0.296 g portion of zinc acetate dehydrate and 12.5 ml of methanol was added to a 50 ml three-neck flask. The solution was heated to 60 °C under vigorous stirring. Then, 0.152 g of potassium hydroxide (KOH) was dissolved in 6.5 ml of methanol. The KOH solution was added to the zinc acetate solution dropwise in about 5 min. The solution was kept at 60 °C for 2 h.

The solution changed to whitish after 1–1.5 h. The heating mantle was removed after 2 h. The solution cooled down to room temperature naturally. The solution was centrifuged. The supernatant was discarded, and the precipitate was cleaned with methanol three times. The precipitate was then dissolved in 4 ml of chloroform:methanol 1:1 solution. The solution was stored at ambient conditions.

LED fabrication

Sapphire substrates were cut into 12.5 mm × 12.5 mm pieces and cleaned by sonication in 2% Alconox solution, acetone and isopropanol for 15 min, respectively. Then, 40 nm ITO was sputtered over the substrate at 10^{-8} Torr. A 4 mm wide strip of tape was manually cut and used to cover the ITO down the middle of the substrate. The substrate was exposed to HCl vapour for 15 s and rinsed with distilled water. The tape mask was then removed, and the remaining ITO was annealed at 300 °C in a quartz tube furnace for 1 h, yielding an electrode with a square resistance of ~80 ohm.

The ZnO solution was spin coated at a speed of 2,000 r.p.m. for 30 s. Three layers of ZnO solution were spin coated in total to achieve a thickness of 60 nm. The substrate was then annealed at 260 °C on a hotplate for 2 min.

A 2% poly(diallyldimethylammonium chloride) in water solution was dropped to cover the film for 10 s to help quantum dots bind to the surface. The film was rinsed with distilled water and dried with nitrogen. The substrate was heated to 35 °C. Two drops of HgSe–CdSe quantum dots solution were drop cast on the substrate with a glass Pasteur pipette. The solution was lightly swirled to keep covering the substrate, before wicking. A 5% 1,2-ethanedithiol in IPA solution was dropped to cover the film for 10 s. The film was rinsed with IPA and dried with nitrogen. The procedure was repeated to reach the desired film thickness. The substrate was then annealed at 150 °C on a hotplate for 5 min.

A 10 mg portion of poly(9-vinylcarbazole) was dissolved in 2 ml of chlorobenzene. The solution was spin coated at a speed of 1,600 r.p.m. for 30 s. Then, 200 nm Ge, 15 nm Pt and 20 nm Au were evaporated at 10^{-8} Torr by electron beam through a mask.

PL measurements

PL spectra were recorded using a similar procedure to that previously reported[32]. The samples were excited with an 808 nm laser diode modulated by a sine wave at 90 kHz. The signal was collimated by a gold-coated f/2 parabolic mirror and sent through a step-scan Michelson interferometer to a cooled HgCdTe detector. A silicon wafer was placed in front of the detector to filter out the laser. The detector output was sent through a lock-in amplifier. The interferometer was controlled by a step motor and scanned to give spectra with 50 cm^{-1} resolution after Fourier transformation.

EL measurements

The device was tested using a Keithley model 6221 a.c. and d.c. current source. A sine wave modulated at 9 kHz with 0 mA to a peak current was applied to the sample. The EL spectra were measured using the same set up as for PL. The peak voltage was measured by viewing the voltage change on an oscilloscope and taking the maximum value.

EQE determination

The PL EQE was determined using a similar procedure to that reported previously[32]. An absolute PL EQE measurement was made for an undoped HgSe–CdSe sample on film using a Spectralon integrating sphere and a PbSe detector. The PL spectrum of this sample was taken. The measured spectrum was normalized by the ratio of a measured and calculated black-body photon flux. The PL EQE per unit spectrum area ratio was then calculated. The PL EQE values of other samples were determined by taking a spectrum, normalizing to black-body photon flux and absorbed laser power and calculating using the ratio described above. The EL EQE was determined in the same way using the injected electron number instead of absorbed photon number.

Data availability

The data that support the findings of this study are available from the corresponding authors upon reasonable request.

Acknowledgements
X.S. is supported by NSF-ECCS-2226311. A.K. is supported by DOE DE-SC0 023210. This work made use of the shared facilities at the University of Chicago Materials Research Science and Engineering Center, supported by National Science Foundation under award number DMR-2011854, and the University of Chicago electron microscopy facility (RRID:SCR_019198).

Author contributions
P.G.S. and X.S. conceived the project. A.K. synthesized the HgSe–CdSe quantum dots. X.S. fabricated and characterized the LED devices. All authors contributed to the discussions of the paper.

Competing interests
The authors declare no competing interests.

Additional information
Supplementary information The online version contains supplementary material available at https://doi.org/10.1038/s41566-023-01270-5.

Correspondence and requests for materials should be addressed to Philippe Guyot-Sionnest.

Peer review information *Nature Photonics* thanks the anonymous reviewers for their contribution to the peer review of this work.